Electronic Supplementary Information

Rapid photoprinting of piezoelectric solid polymer electrolytes for scalable structural energy storage composites

Žan Simon,[*a1] Timothy Harte,[ab1] Anna Demeraux,[a] Ben Newman,[a] Piers Coia,[a] Nilupuli C. Rathnayaka,[a] Daniel J. Eyckens,[b] Bhagya Dharmasiri[*a] and Luke C. Henderson[*a]

[1] These authors contributed equally to this work.

[a] Institute for Frontier Materials, Deakin University, Waurn Ponds, Victoria 3216, Australia

[b] Manufacturing, Commonwealth Scientific and Industrial Research Organisation, Clayton, Victoria 3168, Australia

[*] Corresponding authors. E-mail addresses: luke.henderson@deakin.edu.au (L.C. Henderson); k.dharmasiri@deakin.edu.au (B. Dharmasiri); zsimon@deakin.edu.au (Ž. Simon)

Supplementary Note: Electrochemical Characterisation

Ionic Conductivity

The ionic conductivity (δ) was determined using Equation S1.

$$\delta = \frac{d}{R_b S} \#(1)$$

where *S* refers to the surface area of the sample that is in contact with the electrodes, *d* is the thickness of the electrolyte sample, and *Rb* represents the bulk resistance of the sample.

Table S1. Ionic conductivity calculated values for 3D printed and mould-cured UV resin SPE samples at varying wt.%. N=5.

Sample	Ionic Conductivity±SD (mS cm^{-1})
60% SIL UV 3D	0.0160 ± 1.96E-09
70% SIL UV 3D	0.0435 ± 6.39E-09
80% SIL UV 3D	0.2521 ± 1.52E-08
55% SIL UV	0.0073 ± 1.28E-09
60% SIL UV	0.0117 ± 1.72E-09
70% SIL UV	0.0401 ± 6.81E-09
80% SIL UV	0.1995 ± 1.46E-08
90% SIL UV	0.7831 ± 1.58E-07

Electrochemical Stability Window of the SPE - Cyclic Voltammetry (CV)

The electrochemical stability window of the SPE was determined *via* a stepwise increase in upper voltage limit in a cyclic voltammetry experiment, up to 1.5 V.

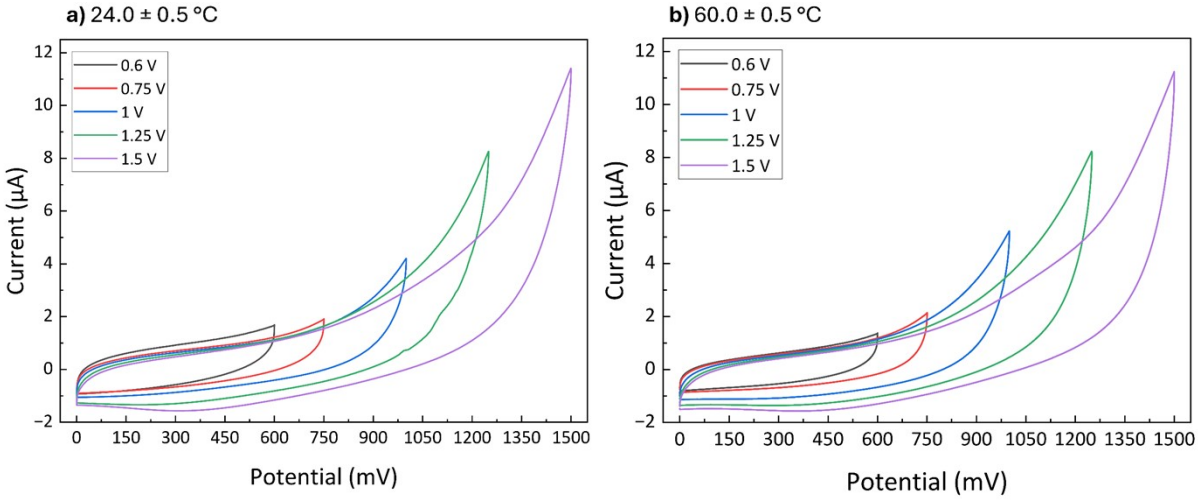

Figure S1. Cyclic voltammograms of the 70% SIL UV 3D sample, at (a) RT of 24.0 ± 0.5 °C, and (b) cycled at 60.0 ± 0.5 °C, at a scan rate of 10 mV s^{-1}. N=3.

Cyclic Voltammetry of Structural Supercapacitor Devices (CV)

SSCs were tested at 100, 50, 20, 10, 5 and 1 mV s^{-1} scan rates with an electric potential window of 0.6 V. Specific capacitance values from CV were determined using Equation S2.

$$C_{CV} = \int \frac{Idv}{m\,\upsilon\,\Delta V} \#(2)$$

where C_{CV} (F g^{-1}) is the specific capacitance, $\int Idv$ (AV) is the area of the cyclic voltammogram corresponding to discharge processes (*i.e.,* half of total area), m (g) is the CF mass of both electrodes, υ (V s^{-1}) is the scan rate, and ΔV (V) is the potential window of the CV.

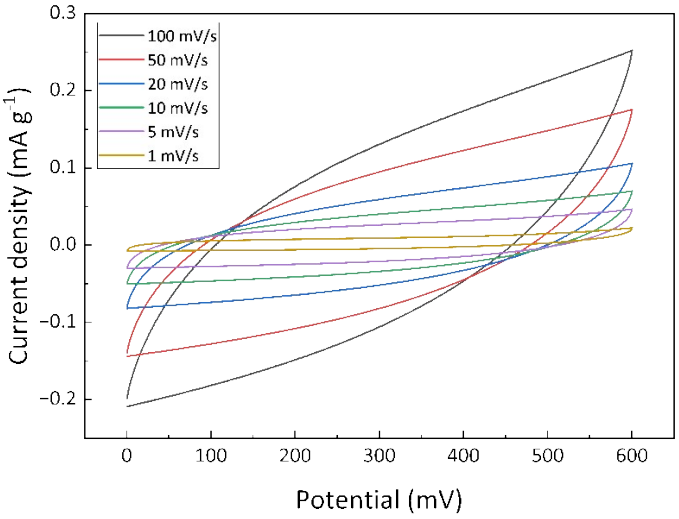

Figure S2. Cyclic voltammogram of a DAQ-functionalised supercapacitor device with the printed layer simultaneously acting as the solid polymer electrolyte and a separator.

Galvanostatic Charge-Discharge (GCD)

GCDs were measured at different discharge current densities with an electric potential window of 0.6 V. Specific capacitance values from GCD were determined using:

$$C_{GCD} = \left(\frac{I_D}{m}\right)\frac{t_D}{\Delta V - V_{IR}} \#(3)$$

where C_{GCD} (F g^{-1}) is the specific capacitance, I_D (A) is the discharge current, t_d (s) is the discharge time, m (g) is the CF mass of both electrodes, and ΔV (V) is the potential window of the GCD test. Since voltage drop due to internal resistance IR (Ω) is inevitable in GCD tests, V_{IR} has been excluded in the calculations for more accurate results due to internal resistance. GCD tests were performed at different discharge currents densities (I_D/m) (A g^{-1}).

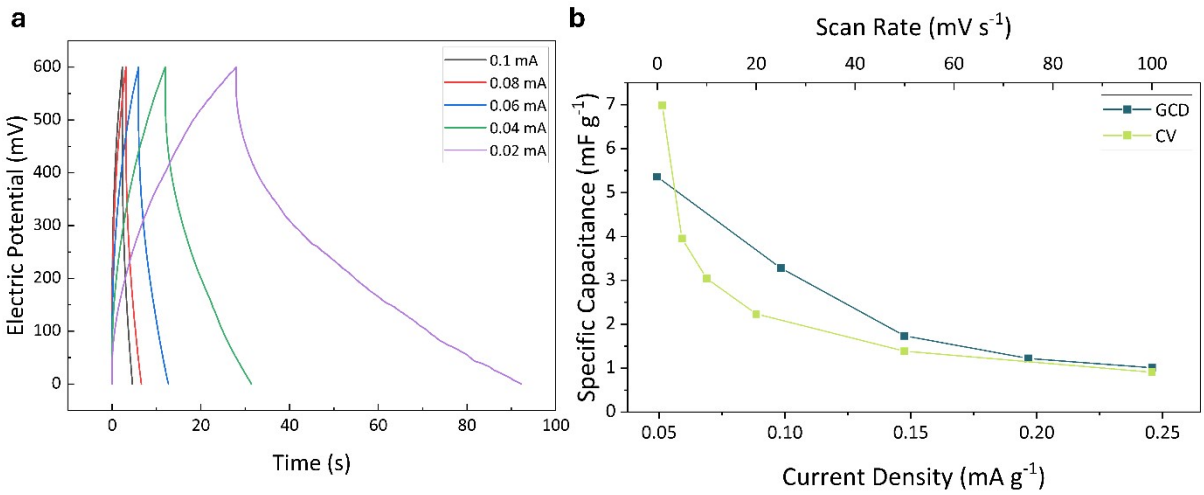

Figure S3. (a) Galvanostatic charge-discharge profiles at varying current limits; (b) Specific capacitance from GCD and CV.

Electrochemical Impedance Spectroscopy (EIS)

For electrochemical impedance spectroscopy (EIS) experiments the frequency was swept from between 10 mHz to 100 kHz with 10 points per decade and a sinus amplitude of 10 mV. EIS data was analysed and circuit Zfit (Figure S6) performed using EC-Lab v11.42 software.

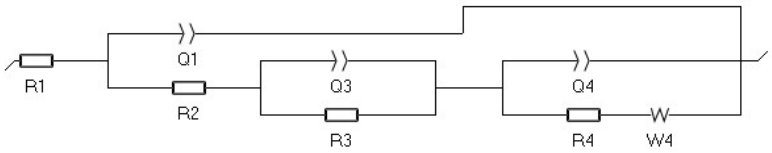

Figure S4. Equivalent electrical circuit used for EIS fitting of the data, representing bulk resistance of the polymer electrolyte (R1), double layer formation (Q1), contact resistance between the polymer electrolyte and carbon fiber interface (R2), bulk capacitance of the polymer electrolyte (C3), and resistance to ion movement through the polymer matrix (R3). Q4/R4/W4 combination represents processes of ion movement through both the polymer and the CF pore network, with capacitance from pores that are partially filled with polymer electrolyte represented in Q4, and the diffusional resistance element (W4; Warburg impedance) being in series with charge transfer resistance (R4).

Table S2. Equivalent circuit EIS parameters for the proof-of-concept supercapacitor device.

Before CV	After CV
R1 = 16.04 Ohm	R1 = 18.35 Ohm
Q1 = 1.065e-9 F.s$^{(a-1)}$	Q1 = 1.574e-9 F.s$^{(a-1)}$
a1 = 0.9455	a1 = 0.9204
R2 = 174.70 Ohm	R2 = 110.30 Ohm
C3 = 1.168e-3 F	C3 = 3.42e-3 F
R3 = 11241 Ohm	R3 = 85144 Ohm
Q4 = 0.71e-3 F.s$^{(a-1)}$	Q4 = 8.547e-4 F.s$^{(a-1)}$
a4 = 0.1085	a4 = 0.06717
R4 = 2.079e-6 Ohm	R4 = 74.15 Ohm

s4 = 7530 Ohm.s$^{-1/2}$	s4 = 8266 Ohm.s$^{-1/2}$
$\chi^2/\|Z\|^2$ = 0.0667	$\chi^2/\|Z\|^2$ = 0.0381

Figure S5. Photo of one electrode just prior to sealing within an aluminium pouch, showing the hexagonal pattern, CF fabric coated with BSPE, frame, and aluminium current collector.

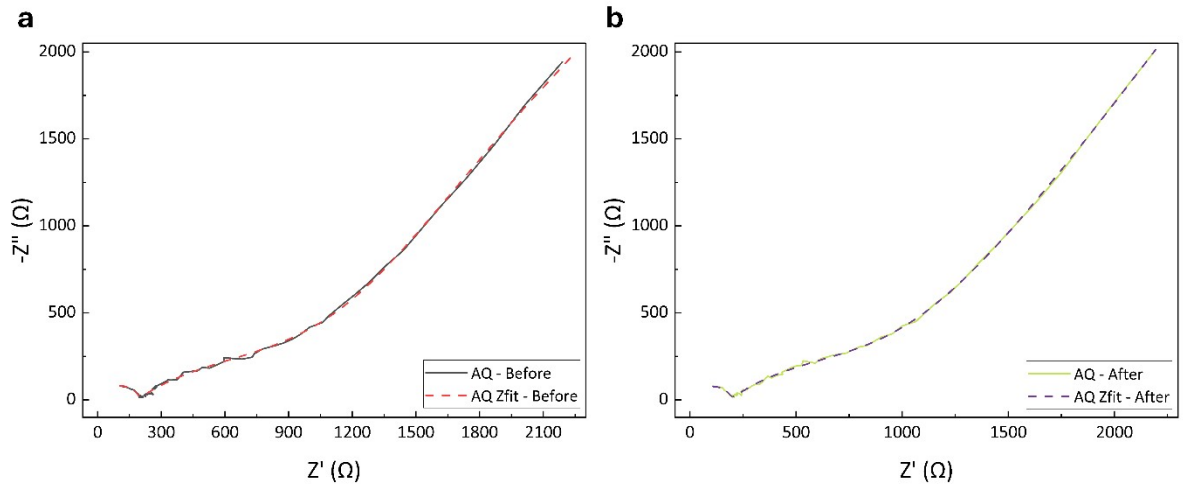

Figure S6. Nyquist impedance from electrochemical impedance spectroscopy on the SSC, *a*) before, and *b*) after cyclic voltammetry experiments.

Supplementary Note: Mechanical Testing

Flexural Testing

The maximum force recorded in the stress-strain curve, right before the force dropped due to failure, and the associated displacement, were utilised to calculate the flexural modulus and flexural strength using Equations S4 and S5, respectively.

$$E_f = \frac{L^3 m}{4bd^3} \#(4)$$

$$\sigma_f = \frac{3FL}{2bd^2} \#(5)$$

where E_f (MPa) represents the flexural modulus, σ_f (MPa) denotes the flexural strength, L (mm) is the span between the supports, d (mm) indicates the depth of the sample, b (mm) refers to the width of the sample, m (N m^{-1}) is the slope of the stress-strain curve, and F (N) represents the maximum force applied.[1]

Tensile Testing

Tensile stress (σ_T) and tensile strain (ε_T) were calculated using Equations S6 and S7, respectively. Young's Modulus (E_T) and Tensile Toughness (U_T) were calculated using Equations S8 and S9, respectively. Polynomial fitting and linear regression for Young's modulus (E_T) determination were automated with a custom Python-v3.11.1 script. Young's modulus (E_T) was calculated in the linear region *via* linear regression using linregress statistical function in the SciPy-v1.9.3 package, using the first 1500 raw data points of the stress-strain curves and capturing the slope for final Young's modulus value. Tensile Toughness (U_T) is defined as the area under the stress-strain curve and was calculated *via* polynomial function fitting and definite integration of said function for each sample. Utilising the scientific computing package NumPy-v1.23.5 and its polyfit method, a 4th degree polynomial was fitted to the stress-strain curve. Data points after the maximum load were eliminated to account for a sharp drop in stress due to failure. This function was then integrated using SciPy-v1.9.3 and its integrate method for definite integral computation, with the integral's limits being 0 and tensile strain upon failure (ε_{Tf}) (mm mm^{-1}), while also eliminating the data points after the maximum load, as with the polynomial fitting.

$$\sigma_T = \frac{F}{A} \#(6)$$

$$\varepsilon_T = \frac{\Delta L}{L} \#(7)$$

$$E_T = \frac{\sigma_T}{\varepsilon_T} \#(8)$$

$$U_T = \int_0^{\varepsilon_{Tf}} \sigma_T \, d\varepsilon_T \#(9)$$

where F (N) is measured load, A (mm^2) is the specimen cross-sectional area; σ_T (MPa or N mm^{-2}) is the tensile stress, ε_T (mm/mm) is the tensile strain, ε_{Tf} (mm mm^{-1}) is the tensile strain upon failure, ΔL (mm) is the change in gauge length, L (mm) is the initial gauge length, E_T (MPa or N mm^{-2}) is the tensile (Young's) modulus, U_T (J mm^{-3}) is the tensile toughness or deformation energy, and ε_T (mm mm^{-1}) is the tensile strain upon failure.

Compression Testing

Stress-strain curves were plotted from the load-deformation curves by dividing the maximum compressive load carried by the specimen during the test by the original minimum cross-sectional area of each specimen, similar to tensile stress determination from Equation S6.

Mould cured SPEs

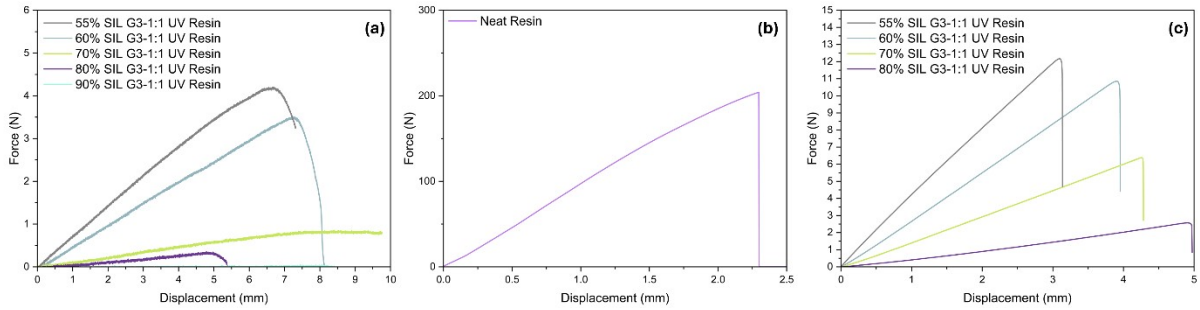

Figure S7. Representative force/displacement break curves for (a) flexural testing of mould cured UV resin SPE samples, (b) mould cured neat UV resin, and (c) tensile testing of mould cured SPE samples.

Table S3. Mechanical properties calculated values for mould cured 55% to 70% UV resin SPE samples.

Property	55% SIL UV	60% SIL UV	70% SIL UV	80% SIL UV	90% SIL UV
Flexural Modulus±SD (MPa)	8.28±1.50	5.73±0.68	4.08±0.33	1.84±0.25	0.30±0.11
Flexural Strength±SD (MPa)	1.58±0.28	0.86±0.30	0.84±0.14	0.33±0.07	0.04±0.01
Young's Modulus±SD (MPa)	3.07±0.40	2.17±0.21	1.06±0.08	0.29±0.06	N/A
Ultimate Tensile Strength±SD (MPa)	1.66±0.45	1.22±0.10	0.72±0.07	0.27±0.06	N/A
Toughness±SD (J mm^{-3})	0.49±0.25	0.33±0.04	0.23±0.05	0.11±0.06	N/A

3D printed SPEs

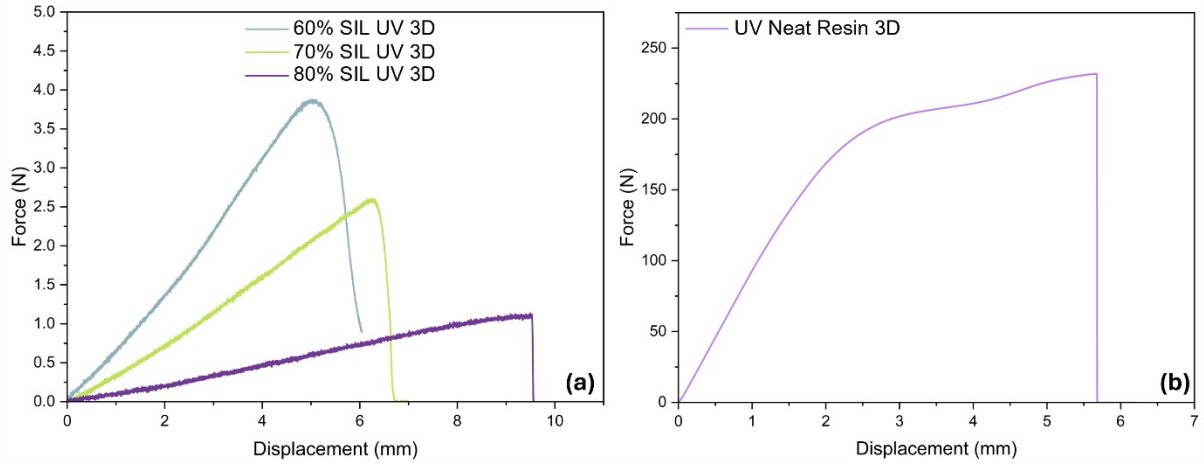

Figure S8. Representative force/displacement break curves for flexural testing of (a) 3D printed UV resin SPE samples, and (b) 3D printed UV neat resin.

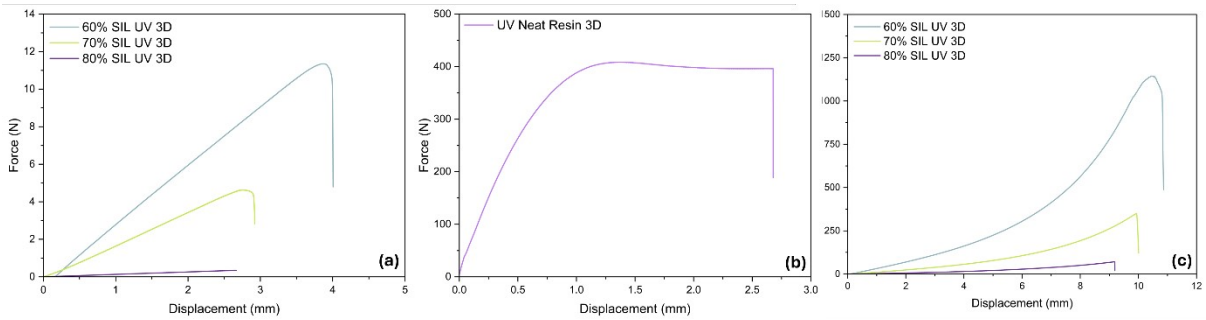

Figure S9. Representative force/displacement break curves for (a) tensile testing of 3D printed SPE samples, and (b) 3D printed neat UV resin; (c) Representative force/displacement curves for compression testing of 3D printed UV resin SPE samples.

Table S4. Mechanical properties calculated values for 3D printed UV resin SPE samples.

Property	60% SIL UV 3D	70% SIL UV 3D	80% SIL UV 3D	Neat 3D Resin
Flexural Modulus±SD (MPa)	11.78±0.55	5.45±0.40	1.86±0.27	398.12±50.00
Flexural Strength±SD (MPa)	1.40±0.11	0.78±0.26	0.35±0.06	62.44±6.55
Young's Modulus±SD (MPa)	2.11±0.39	1.08±0.12	0.23±0.04	450.73±26.15
Ultimate Tensile Strength±SD (MPa)	0.91±0.33	0.20±0.06	0.03±0.01	32.40±2.83
Toughness±SD (J mm^{-3})	0.26±0.05	0.06±0.02	0.01±0.00	8.72±3.19
Ultimate Compressive Strength±SD (MPa)	10.69±1.59	3.07±0.32	0.58±0.15	N/A

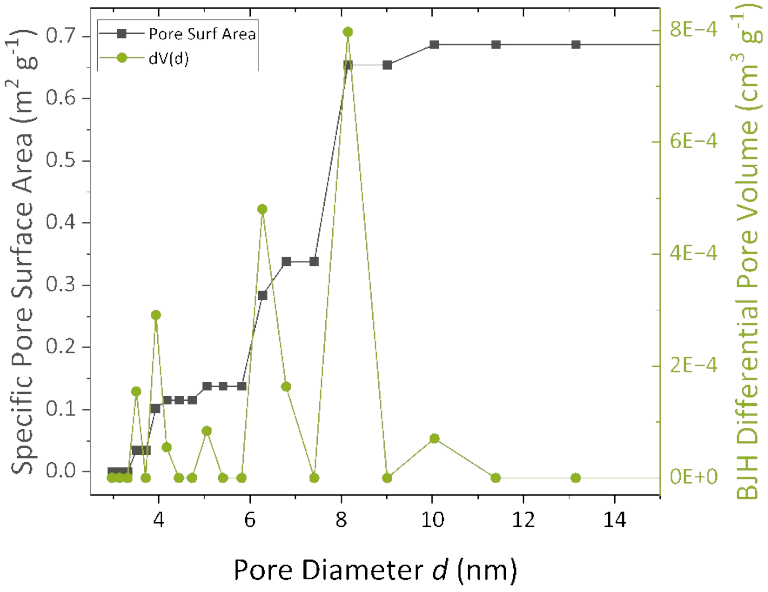

Figure S10. BJH nitrogen gas adsorption analysis for specific surface area and pore diameter, with a specific surface area recorded of 0.709 m^2 g^{-1}, and a random pore size distribution with the majority at 8.149 nm.

Supplementary Note: Thermal Analysis

Mould-cured SPEs

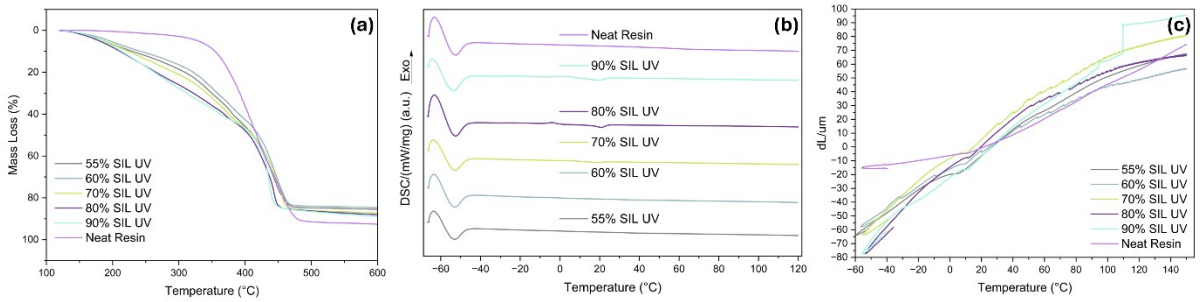

Figure S11. (a) TG curves for all wt.% ratios of SIL mould cured UV Resin samples and UV neat resin; (b) DSC curves for all wt.% ratios of SIL mould cured UV resin samples and UV neat resin; (c) TMA thermal expansion traces for all wt.% ratios of SIL mould cured UV Resin samples and UV neat resin.

Table S5. T_d (°C) values for mould cured UV resin SPE samples.

Sample	T_d (°C)	Mass loss (%)
55% SIL UV	199.4	5.00
60% SIL UV	208.6	5.00
70% SIL UV	199.4	4.99
80% SIL UV	192.9	4.99
90% SIL UV	194.0	5.00
UV neat resin	329.4	4.99

Table S6. TMA transition temperatures for mould cured UV resin SPE samples.

Sample	Transition Temperature (°C)
55% SIL	2.6
60% SIL	N/A
70% SIL	9.5
80% SIL	11.0
90 % SIL	10.1
UV neat resin	44.3 & 77.0

Table S7. Average coefficient of linear thermal expansion (α) for mould cured UV resin SPE samples in the temperature range from -30 °C to 30 °C.

Sample	α (μm °C^{-1})	Sample size (mm)
55% SIL	0.7153	4.56
60% SIL	0.6892	3.81
70% SIL	0.8604	4.02
80% SIL	0.9393	3.80
90% SIL	0.8160	3.83
UV neat resin	0.2585	3.65

No significant trends were observed in decomposition temperature (T_d) or DSC data across mould-cured BSPEs with varying SIL content. All samples exhibited T_d >192 °C (Table S3). DSC curves of mould-cured BSPEs (Figure S11) up to 70% were consistent with the bicontinuous nature and did not show strong glass transitions (Fig. S11). Thermomechanical analysis (TMA) revealed characteristic trends in thermal expansion behaviour across mould-cured BSPEs with varying SIL content (Figure S11, Table S6). The average coefficient of linear thermal expansion calculated over the −30 °C to 30 °C range increased notably with SIL content, from 0.69 µm °C^{-1} at 60% SIL to a maximum of 0.94 µm °C^{-1} at 80% SIL (Table S7). This trend indicates enhanced thermomechanical compliance with increasing incorporation of the liquid SIL phase, which softens the polymer matrix and allows greater dimensional response to thermal stress. A slight decrease at 90% SIL (0.82 µm °C^{-1}) suggests that excessive SIL loading may begin to disrupt phase continuity or over-saturate the polymer network, limiting further expansion. These findings are characteristic of BSPEs, where expansion behaviour does not scale linearly with filler content as seen in single-phase materials, due to the interplay between polymer-rich and SIL-rich domains.

3D printed SPEs

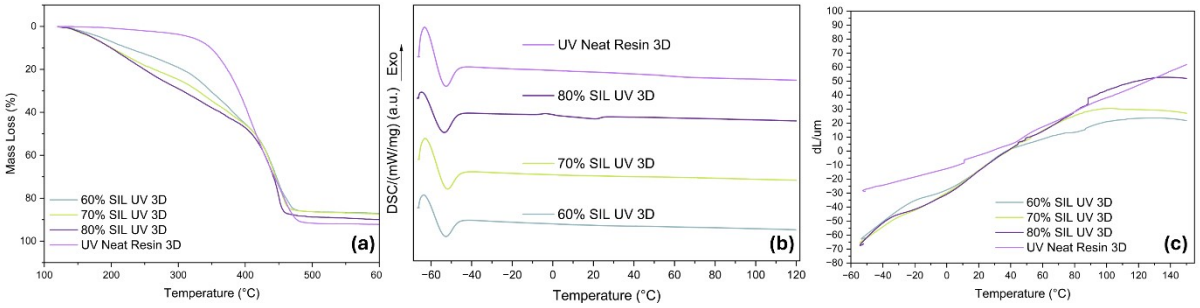

Figure S12. (a) TG curves for 60%, 70% & 80% wt.% 3D printed SPE samples and 3D printed UV neat resin; (b) DSC curves for 60%, 70% & 80% wt.% 3D printed SPE samples and 3D printed UV neat resin; (c) Thermal expansion curves for 60%, 70% & 80% wt.% 3D printed SPE samples and 3D printed UV neat resin.

Table S8. Degradation temperature values for 3D printed UV resin SPE samples.

Sample	T_d (°C)	Mass loss (%)
60% SIL	199.9	5.00
70% SIL	188.3	5.00
80% SIL	186.5	5.01
Neat Resin 3D	321.1	5.01

Table S9.TMA transition temperatures for 3D printed SPE samples.

Sample	Transition Temperature (°C)
60% SIL	-11.3
70% SIL	-22.7
80% SIL	-26.8
Neat Resin 3D	47.7

Table S10. Average coefficient of linear thermal expansion (α) figures for 3D printed SPE samples in the temperature range from -30 °C to 30 °C.

Sample	α (μm °C^{-1})	Sample size (mm)
60% SIL	0.6152	3.58
70% SIL	0.6851	3.79
80% SIL	0.6536	3.50
Neat Resin 3D	0.3726	3.76

The decomposition temperatures (T_d) of 3D printed BSPE samples were >186 °C across all compositions, slightly lower than those of mould cured UV resin SPEs (Table S6). This minor reduction of <4% indicates no significant change in the thermal stability behaviour of the SPEs and resins between the mould and 3D printed curing techniques.

DSCs of the mould cured, and 3D printed SPE samples (Figures S11, S12) indicated no significant change in the thermal phase behaviour of the SPEs and resins between the mould and 3D printed curing techniques. The TMA transition temperatures and linear thermal expansion coefficients reveal notable differences between 3D printed and mould cured UV resin-based SPEs. The 3D printed SPEs displayed significantly lower transition temperatures, with values ranging from -11.3 °C to -26.8 °C for the 60-80 wt.% SIL-containing samples (Table S7). In contrast, the positive transition temperatures were observed in mould cured samples (***e.g.***, 2.6 °C for 55% SIL and 11.0 °C for 80% SIL, Table S4). The significantly lower transition temperatures observed in the 3D printed SPEs, compared to their mould-cured counterparts, can be attributed to differences in the homogeneity of mixing during fabrication. In the 3D printing process, the initial high shear mixing of the SIL with the resin followed by the localised and rapid curing conditions results in enhanced homogeneity. This significantly reduces the interactions between polymer chains, thereby enhancing chain mobility even at sub-zero temperatures. In contrast, mould cured samples undergo bulk curing, which can result in less uniform distribution of the ionic liquid, potentially leading to localized SIL-rich and polymer-rich domains. As a result, large regions of the polymer matrix remain relatively rigid, that dominate the thermal response of the system, leading to higher transition temperatures despite the presence of SIL.[2-6] The improved thermal stability and more distinct transition features in 3D printed samples were attributed to the spatially controlled nature of curing during printing. This gradual and localised exposure allows better heat dissipation and minimises the risk of exotherm-induced bubble formation. Accordingly, the rougher thermal expansion profiles observed for the mould cured SPEs are consistent with the presence of voids and heterogeneous domains, which disrupt the matrix response under thermal stress. In contrast, the smoother thermal expansion curves of the 3D printed samples reflect a more homogeneous microstructure, enabled by the precise control of light exposure and improved heat management during curing.[2-5]

Diazotised DAQ and DAQ-CF

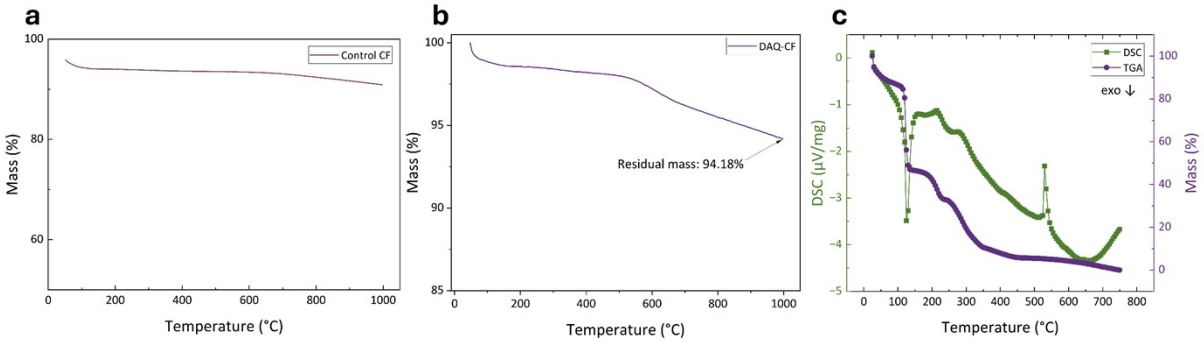

Figure S13. a) TGA trace of the control, unsized CF; b) TGA trace of the DAQ-functionalised CF; c) STA trace of the diazotised DAQ powder.

Supplementary Note: Piezoelectric Testing

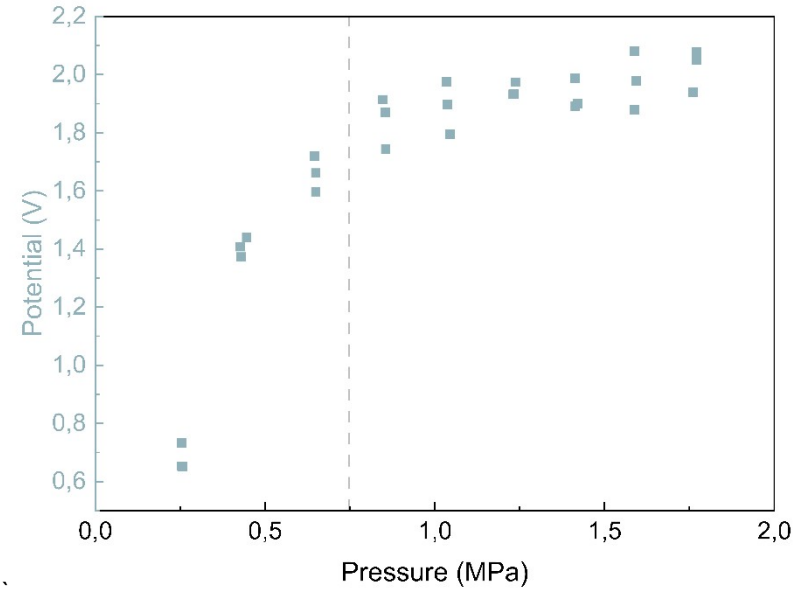

Figure S14. Voltage as a function of pressure for higher pressures, up to 1.77 MPa. Dashed line showing a rough estimate for the limit of linear voltage increase with pressure, after which the OCP response showed the exponential behaviour to the horizontal asymptote of maximum electric potential output, likely due to saturation of transient liquid-to-crystalline phase formation.

Table S11. Fitting parameters for line of best fit for potential from Figure 4c.

Parameter	Result
Equation	y = a + b × x
Intercept	0
Slope	3.0303±0.0879
Residual Sum of Squares	64.5510
Pearson's r	0.9971
R-Square (COD)	0.9941
Adj. R-Square	0.9933

Table S12. Fitting parameters for line of best fit for current from Figure 4c.

Parameter	Result
Equation	y = a + b × x
Intercept	0
Slope	1.6178±0.1755
Residual Sum of Squares	559.6730
Pearson's r	0.9612
R-Square (COD)	0.9238
Adj. R-Square	0.9130

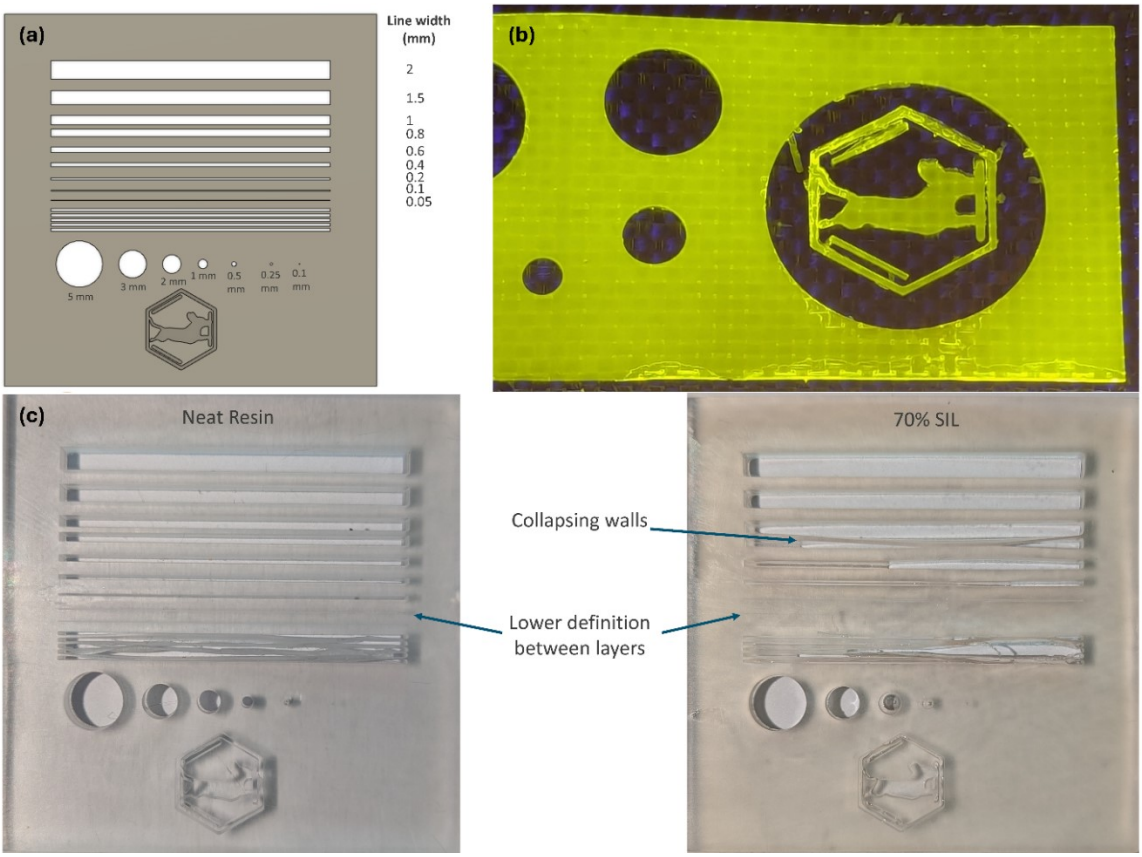

Figure S15. Initial prints for dimensional fidelity investigation. (a) CAD model of the test print; (b) Successful printing with satisfactory adhesion to CF fabric, with exposure to UV light to check for uniformity; (c) Printed neat resin design (left) and 70% SIL UV 3D (right).

References

1. C. Zweben, W. Smith and M. Wardle, 1979.
2. M. S. Grewal, K. Kisu, S.-i. Orimo and H. Yabu, Photo-crosslinked polymer electrolytes containing solvate ionic liquids: an approach to achieve both good mechanical and electrochemical performances for rechargeable lithium ion batteries, *Chem. Lett.*, 2020, **49**, 1465-1469. 10.1246/cl.200572.
3. S. Sirovica, Y. Guo, R. Guan, M. W. Skoda, W. M. Palin, A. P. Morrell, D. L. Romanyk, R. A. Martin and O. Addison, Photo-polymerisation variables influence the structure and subsequent thermal response of dental resin matrices, *Dent. Mater. J.*, 2020, **36**, 343-352. 10.1016/j.dental.2019.12.004.
4. A. Kowalska, J. Sokolowski and K. Bociong, The photoinitiators used in resin based dental composite—a review and future perspectives, *J. Polym.*, 2021, **13**, 470. 10.3390/polym13030470.
5. J. Kloosterboer and G. Lijten, Thermal and mechanical analysis of a photopolymerization process, *Polym. J.*, 1987, **28**, 1149-1155. 10.1016/0032-3861(87)90258-8.
6. V. Mucci, G. Arenas, R. Duchowicz, W. D. Cook and C. Vallo, Influence of thermal expansion on shrinkage during photopolymerization of dental resins based on bis-GMA/TEGDMA, *Dent. Mater. J.*, 2009, **25**, 103-114. 10.1016/j.dental.2008.04.014.